Available online at www.sciencedirect.com
ScienceDirect
Acta Materialia 78 (2014) 37–45
Acta MATERIALIA
www.elsevier.com/locate/actamat

Stress, temperature and electric field effects in the lead-free $(Ba,Ca)(Ti,Zr)O_3$ piezoelectric system

Matthias C. Ehmke [a,*,1], Florian H. Schader [b], Kyle G. Webber [b], Jürgen Rödel [b], John E. Blendell [a], Keith J. Bowman [a,c]

[a] School of Materials Engineering, Purdue University, West Lafayette, IN 47907, USA
[b] Institute of Materials Science, Technische Universität Darmstadt, 64287 Darmstadt, Germany
[c] Mechanical, Materials & Aerospace Engineering, Illinois Institute of Technology, Chicago, IL 60616, USA

Received 19 March 2014; received in revised form 27 May 2014; accepted 2 June 2014
Available online 16 July 2014

Abstract

The large signal strain response as a function of uniaxial compressive stress, electric field and temperature is investigated for compositions across the morphotropic phase boundary in the $(Ba,Ca)(Ti,Zr)O_3$ ferroelectric system. The largest piezoelectric coefficient in terms of unipolar strain divided by the maximum applied field, S_u/E_{max}, is 1540 pm V^{-1}, which clearly exceeds the piezoelectric response of most lead zirconate titanate materials. The extraordinarily large piezoelectric properties occur in the vicinity of the morphotropic phase boundary region on the rhombohedral side of the phase diagram. In this material, an electric threshold field is observed that is required to overcome the stress-induced domain clamping and obtain a measurable strain response. Moreover, the study reveals that careful selection of composition, stress and field amplitude allow for large signal piezoelectric coefficients of over 740 pm V^{-1} in the temperature range of 25–75 °C. The extraordinarily large unipolar strain response can be assigned to an electric field-controlled regime, in which the unipolar compressive stress induces non-180° domain switching perpendicular to the applied electric field. During electrical loading, the electric field can realign these domains back into the parallel direction, maximizing non-180° domain switching and enhancing unipolar strain.

Keywords: BZT-BCT; Lead-free; Ferroelectrics; Actuator; Ferroelasticity

1. Introduction

Piezoelectric materials are used in a variety of applications, prominently as actuators, sensors and electromechanical transducers [1–3]. The material of choice for these applications in the past 60 years has been lead zirconate titanate (PZT), because it offers large piezoelectric coefficients, excellent electromechanical performance, a range of properties tunable through doping, and a well-studied and reliable ceramic processing route [1–3]. The global market for piezoelectric actuators alone was reported to be US$6,587 million in 2009, with bulk PZT materials having a market share of over 98% [4]. These numbers are expected to almost double by 2014, when bulk PZT is expected to remain the dominant material with over 95% of the market [4]. This is despite the legislative measures pushed forward by many countries and states, such as the EU [5,6], Japan [7], China [8], Korea [9] and California [10], to minimize and ultimately ban the use of toxic compounds in electronic equipment.

* Corresponding author.
E-mail address: ehmke@purdue.edu (M.C. Ehmke).
[1] Work performed at Institute of Materials Science, Technische Universität Darmstadt, Germany.

http://dx.doi.org/10.1016/j.actamat.2014.06.005
1359-6454/

The search for lead-free alternatives, triggered by the report by Saito et al. in 2004 [11], has led to the development of two major classes of materials that have been heavily investigated and are based on (K,Na)NbO_3 and ($Bi_{0.5}Na_{0.5}$)-TiO_3 (BNT) [12–14]. More recently, the report by Liu and Ren [15] on the Ca^{2+}- and Zr^{4+}-substituted barium titanate ((Ba,Ca)(Ti,Zr)O_3; BCTZ) system with piezoelectric coefficients of more than 600 pm V^{-1} has increased research interest. The large signal piezoelectric response, expressed as the unipolar strain divided by the maximum field, S_u/E_{max}, was reported to exceed 1200 pm V^{-1} at 0.5 MV m^{-1} in the stress-free state [16]. This exceptional piezoelectric performance under comparatively small electric fields is ascribed to the presence of the strongly temperature-dependent morphotropic phase boundary (MPB). At the MPB, evidence of the coexistence of rhombohedral $R3m$ and tetragonal $P4mm$ phases [15,17] and an additional intermediate orthorhombic $Amm2$ phase [18,19] has been reported. This can enable a large piezoelectric response through the polarization rotation and extension mechanisms originating from a flattening of the energy landscape [12,15,20]. One major limitation of this system is the comparatively low Curie point, T_c, of approximately 100 °C, at which the ferroelectric to paraelectric phase transition occurs.

Electromechanical applications, such as stack actuators, require large field-induced displacements as well as the development of a large force during actuation that can act against external elements [1,21,22]. In order to evaluate how the material performs against external mechanical constraints, the blocking force can be determined. By definition, it is the maximum force at a given electric field acting against an infinitely stiff external clamping and is used by actuator manufactureres as a figure of merit [23–27]. Experiments conducted on soft PZT- and BNT-based materials demonstrate the corresponding blocking forces [24,25]. It must be noted, however, that these experiments represent quasi-static behavior. A real-world scenario constitutes the dynamic interplay between mechanical stress and electric field application acting on the obtainable strain response. Here, unipolar electric field measurements under constant stress for compositions across the MPB in the BCTZ system are reported. The stress- and electric-field-dependent properties at different temperatures are analyzed and contrasted to previous experiments on soft PZT- and BNT-based materials to give insight into the viability of this material system for actuator applications [26,27].

2. Experimental

BCTZ materials with the chemical formula $(1-x)Ba(Zr_{0.2}Ti_{0.8})O_3 - x(Ba_{0.7}Ca_{0.3})TiO_3$ were produced using a solid oxide and carbonate processing route. The compositions are $x = 0.4$ (40BCT), $x = 0.5$ (50BCT) and $x = 0.6$ (60BCT) [15–19,28]. The starting materials were high-purity $BaZrO_3$ (99.5%, Sigma Aldrich), $CaCO_3$ (99.0%, Sigma–Aldrich), $BaCO_3$ (99.8%, Alfa Aesar) and TiO_2 (99.8%, Sigma–Aldrich). The starting powders were ball-milled for 24 h in ethanol, dried, calcined for 2 h at 1350 °C, ball-milled for another 24 h in ethanol, dried and the resulting agglomerates broken up with a ceramic mortar and pestle. The ceramic powders were passed through a 70-mesh (0.212 mm) sieve, before they were compacted using a double-acting uniaxial pressing die. Sintering was carried out for 5 h in air at 1450 °C. The phases present were confirmed by X-ray diffraction (XRD) using a Bruker D8 Focus diffractometer with Cu K_α radiation. The compositions at room temperature span from single-phase rhombohedral (40BCT) through one variant of phase mixtures of rhombohedral, tetragonal and orthorhombic (50BCT) to single-phase tetragonal (60BCT). The sintered ceramics were machined to cylinders with a height of 6 ± 0.02 mm and a diameter of 5.8 ± 0.02 mm. Prior to testing, the samples were annealed at 400 °C to depolarize the materials. Silver electrodes were applied using sputter coating.

The electromechanical experiments were carried out using a screw-type load frame (Zwick Roell Z010) with a customized sample environment that allows the simultaneous application of compressive mechanical stresses and electric fields at elevated temperature up to 800 °C. A thermocouple is positioned in the base of the sample holder approximately 6 mm from the sample that was used to regulate the temperature. The experimental setup and the reproducibility of the measurements are presented in detail elsewhere [25,29]. Electric fields were applied using an arbitrary waveform generator (Agilent 33220) connected to a high-voltage power supply (TREK 20/20C). The strain was measured using a linear variable differential transformer located outside of the heating chamber. Various other experimental arrangements have previously been used to investigate the electric-field-dependent ferroelasticity of PZT [30–34], although these setups have typically relied on the use of strain gages, which has limited the application of temperature [35].

A virgin sample was used for measurements at 25 °C. The contact stress, i.e. the smallest stress applied without losing contact to the sample, was $\sigma_0 = 3$ MPa using a force control mode. Note that the minus sign is omitted as only compressive stresses are considered during the following discussion. Nine consecutive triangular unipolar electric field cycles were applied at a frequency of 50 mHz, where the first three cycles had a field amplitude of 2 MV m^{-1}, the next three cycles had a field amplitude of 1 MV m^{-1} and the last three cycles had a field amplitude of 0.5 MV m^{-1}. In that way, the cycling at 2 MV m^{-1} determines the amount of poling and the consecutive cycles at lower fields probe the response under the same poling conditions at smaller electric fields. For each field amplitude, the third cycle was used for data analysis. The mechanical load was subsequently increased stepwise to 250 MPa. At each stress level the same nine consecutive electric field cycles were applied and the strain was measured. The displacement sensor zero point was referenced to the electrically unloaded state at the contact stress, which allowed for determination of the stress induced displacement. No significant strain drift was observed during testing; small changes originating from time-dependent domain processes were found to be negligible. Following testing at the largest stress, the measurement at 3 MPa was repeated to exclude the possibility of electric fatigue. No difference can be observed between the first measurement and the one after the complete testing cycle. After completing the measurements at 25 °C, the temperature was sequentially increased to 50, 75 and 100 °C. At each temperature, the same measurements were performed under the same mechanical load steps. The accuracy of the temperature near the sample in the heating chamber was ±2 °C. Performing measurements at 3 MPa on different samples of the same composition revealed strain deviations of less than 10%. The test setup was shown to produce accurate measurements with experimental errors of ±5% [29].

3. Results and discussion

3.1. Stress-dependent strain measurements

Fig. 1a–c provides the stress-dependent electric-field-induced strains for 40BCT, 50BCT and 60BCT (from top to bottom), respectively, at 25, 50, 75 and 100 °C (from left to right). Curves up to 100 MPa are provided. The strains at the different field amplitudes are black, red and blue for 2, 1 and 0.5 MV m^{-1}, respectively. The remnant strain at 3 MPa, $S_r(\sigma_0)$, is defined as zero. All strain loops at stresses $\sigma > \sigma_0$ are relative to that and are shifted towards negative strains as a response to the increasing compressive stress. It is apparent from Fig. 1 that the slopes of the strain loops depend significantly on composition. While, for small stresses in 40BCT, the slope of the strain dramatically decreases with increasing electric fields, it is almost field-independent in 60BCT. At large stresses, the strain is zero under small electric fields in 40BCT, while there is always a finite strain component in 50BCT and 60BCT, even at the largest stresses. With increasing temperature, the amount of stress-induced strain is reduced, which can be seen from the strain curves approaching each other. In addition, the field-induced strain decreases with temperature as the materials approach T_c.

The reduction in electric-field-induced strain under compressive stress (Fig. 1) can be primarily attributed to domain clamping in the direction perpendicular to the applied electric field and stress. In 40BCT, for example, a compressive stress of 100 MPa reduces the strain response to zero at electric fields below approximately 1.3 MV m^{-1} at room temperature (Fig. 1a)). The field required to initiate unipolar strain is defined here as the threshold field, E_{thr}. This is unlike PZT [26], BNT-BT [27] or the 50BCT (Fig. 1b)) and 60BCT (Fig. 1c)) compositions, for which there is always a finite strain observable even under the largest applied stresses. This finite strain can be due to

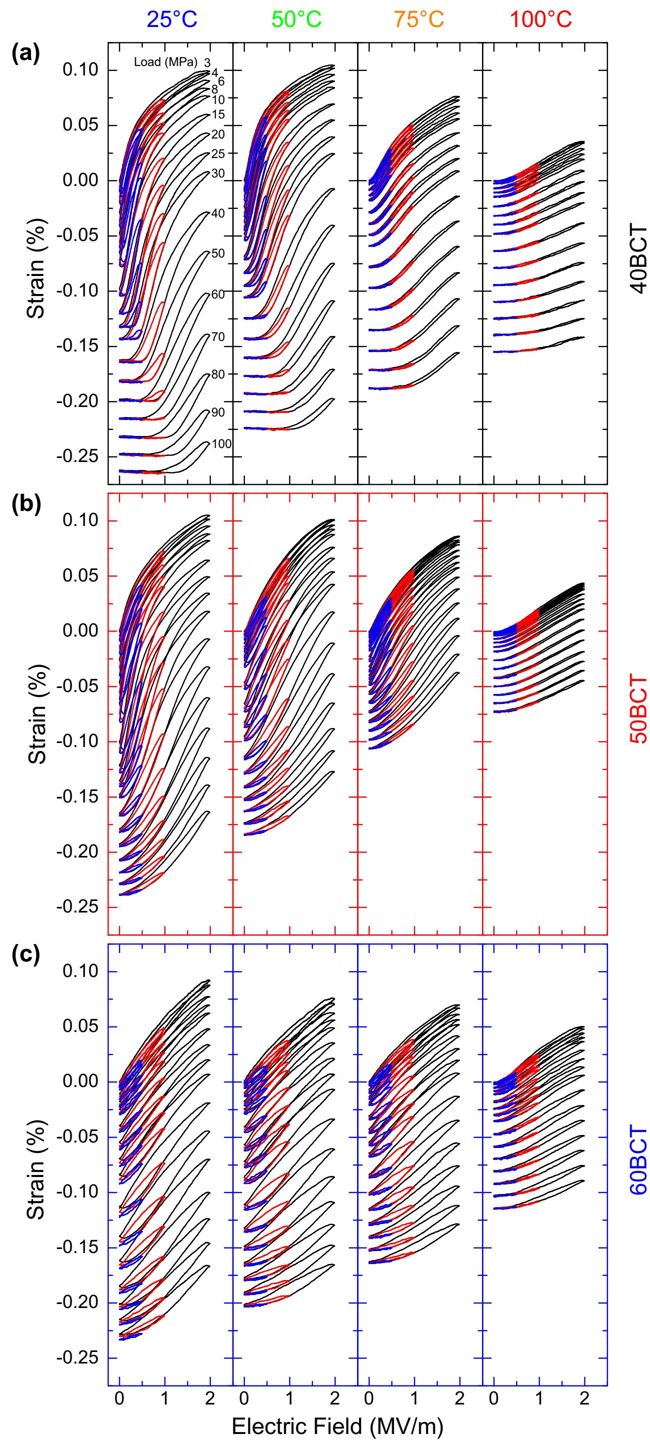

Fig. 1. Stress-dependent electric-field-induced strain at 25, 50, 75 and 100 °C (from left to right) for compositions (a) 40BCT, (b) 50BCT and (c) 60BCT (from top to bottom). The electric field amplitudes are 2 MV m^{-1} (black), 1 MV m^{-1} (red) and 0.5 MV m^{-1} (blue). The maximum compressive stress shown is 100 MPa. (For interpretation of the references to color in this figure legend, the reader is referred to the web version of this article.)

non-180° domain alignment, intrinsic piezoelectricity and electrostriction. This suggests that in 40BCT the stress is responsible for excessive domain clamping, which eliminates the extrinsic strain component. This phenomenon of a threshold field, which is required for the 40BCT material to show a field-induced strain response, is illustrated in more detail in Fig. 2. In Fig. 2a the stress-dependent strain data of 40BCT for an electric field amplitude of 2 MV m^{-1} is provided at 25 °C, where the determined values for E_{thr} are overlaid. E_{thr} can be determined, as illustrated in Fig. 3, from the intersection of two tangents extrapolating the low- and high-field strain responses. At small stresses, $\sigma < 20$ MPa, a threshold field cannot be determined due to the small negative strain contribution. This suggests that the compressive stress results in a domain redistribution after removal of the electric field that can lead to a negative strain once the field is increased again and starts to align the domains in field direction. At 20 MPa, E_{thr} is 0.28 MV m^{-1}, and this increases almost linearly to 1.78 MV m^{-1} at 125 MPa. At 150 MPa and above, the E_{thr} values are larger than 2 MV m^{-1}. E_{thr} as a function of stress and temperature can be seen in Fig. 2b. The E_{thr} values are nearly linear with σ at all temperatures. The slope of E_{thr} with σ decreases with temperature, which coincides with the structural distortions becoming smaller in the vicinity of T_c. As a result, the stress-induced domain clamping can be more easily overcome, because the lattice distortion of the domains that switch by non-180° is smaller. At 100 °C, which is above T_c in 40BCT [15,16], the E_{thr} curve appears shifted towards higher fields, because of the quadratic character of the electrostrictive strain curves [2].

3.2. Optimal working conditions

The large signal piezoelectric coefficient, expressed as $S_u/E_{\max}$, is an effective metric to evaluate the stress-dependent electromechanical performance at the different

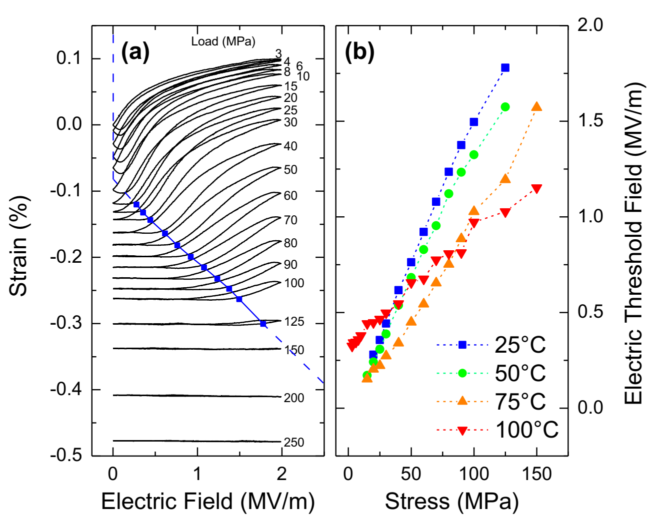

Fig. 2. (a) The stress-dependent electric-field-induced strain is shown for 40BCT. The determined electric threshold field, E_{thr}, at 25 °C is overlaid onto the strain data. It indicates the field strength required to overcome stress-induced domain clamping and develop a measureable strain. (b) The electric threshold field is shown as a function of the applied compressive stress and temperature.

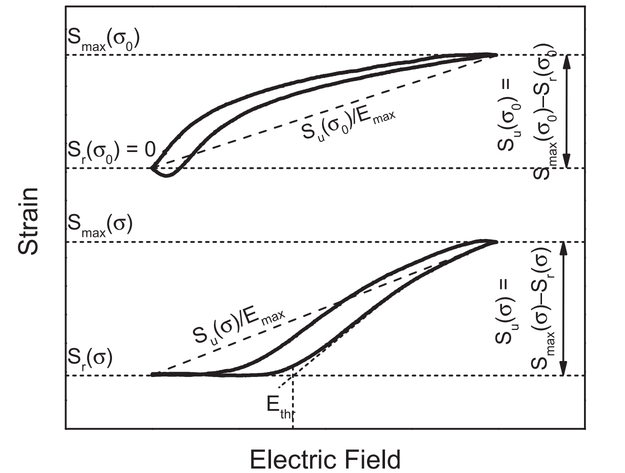

Fig. 3. Schematic defining the different strain quantities, the large signal piezoelectric response $S_u/E_{\max}$ and the electric threshold field E_{thr}.

operating temperatures and to identify the optimal working conditions of the different compositions. Here, the unipolar strain S_u at a given stress σ is

$$S_u(\sigma) = S_{\max}(\sigma) - S_r(\sigma) \tag{1}$$

A schematic with the definitions of the different strains can be seen in Fig. 3. The maximum fields $E_{\max}$ correspond to the electric field amplitudes 2, 1 and 0.5 MV m^{-1}.

Using Eq. (1), the large signal piezoelectric coefficient was characterized for each composition as a function of applied electric field, stress and temperature (Fig. 4). From Fig. 4a it can be seen that the largest $S_u/E_{\max}$ at $\sigma_0 = 3$ MPa in 40BCT is observed for field amplitudes of 0.5 MV m^{-1} except for at 100 °C, where the material is in the paraelectric state. This is also true for 50BCT (Fig. 4b)) at 25 and 75 °C. This observation can be assigned to the large slope in strain at small electric fields compared to larger fields (Fig. 1). At higher stresses, the largest $S_u/E_{\max}$ values are found at 0.5 MV m^{-1} in 40BCT at 25 and 50 °C and in 50BCT at 25 °C, with values between 1420 and 1540 pm V^{-1} for stresses between 8 and 10 MPa. To the best of our knowledge, these are the largest values for the large signal piezoelectric coefficient reported so far in the BCTZ material system, clearly exceeding values for commercial soft PZT materials at these temperatures [26]. For higher electric field amplitudes the maxima exhibit smaller $S_u/E_{\max}$ values due to saturation in the strain–electric field response and are shifted to slightly higher stresses. In 60BCT, the maxima are only weakly pronounced and the same trend persists, i.e. the maxima are shifted to higher stresses at larger field amplitudes. However, the maximum values do not exceed 500 pm V^{-1} and are also not larger at smaller fields, which is consistent with the rather linear strain response in Fig. 1c.

At 25 °C and σ_0, the $S_u/E_{\max}$ for 2, 1 and 0.5 MV m^{-1} are 500, 780 and 1110 pm V^{-1} in 40BCT, 520, 760 and 980 pm V^{-1} in 50BCT and 460, 500 and 460 pm V^{-1} in 60BCT, respectively. The values are reported with an

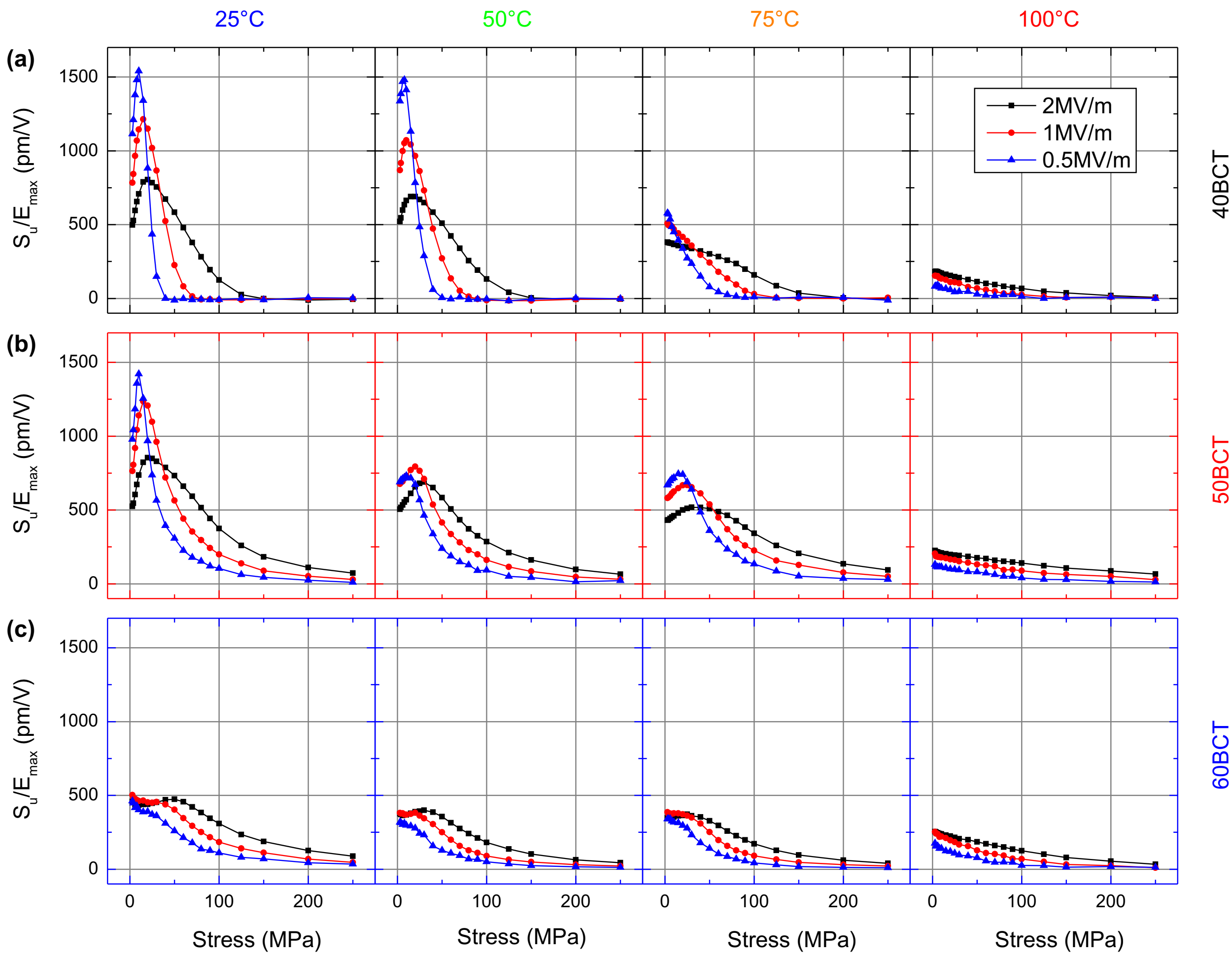

Fig. 4. Large signal piezoelectric response, $S_u/E_{\max}$, as a function of the compressive load at temperatures 25, 50, 75 and 100 °C (from left to right) for compositions (a) 40BCT, (b) 50BCT and (c) 60BCT (from top to bottom). The electric field amplitudes are 2 MV m^{-1} (black), 1 MV m^{-1} (red) and 0.5 MV m^{-1} (blue). (For interpretation of the references to color in this figure legend, the reader is referred to the web version of this article.)

accuracy of $\pm$10 pm V^{-1}. The initial increase in $S_u/E_{\max}$ with increasing stress suggests that domains are aligned perpendicular to the electric field by the stress, which then allows for an increased non-180° domain alignment under field application. At larger stresses it becomes subsequently harder for the electric field to align the domains as they become more and more clamped in the direction perpendicular to the field. The observation of an enhanced unipolar strain with compressive stress, followed by a subsequent decrease, has been previously shown in bulk PZT [33,36] and multilayer PZT [37,38], as well as for BNT-BT bulk materials [27]. As previously noted, the $S_u/E_{\max} \approx 0$ pm V^{-1} for stresses above approximately 150 MPa in 40BCT, as massive domain clamping occurs.

Overall, the electromechanical performance in the 40BCT and 50BCT compositions is significantly superior between 25 and 75 °C than in other lead-free ferroelectrics, such as BNT-BT [27]. Based on the presented data, the careful selection of composition and the adjustment of the stress and electric field profile allows for a large signal piezoelectric coefficient between 740 and 1540 pm V^{-1} for temperatures ranging from 25 to 75 °C.

3.3. Field-free elastic and ferroelastic properties

As described above, the increasing compressive stress causes non-180° domains to switch from the axial to the perpendicular direction, resulting in a ferroelastic strain, $S_{\text{ferroelastic}}$. In Fig. 1, this is reflected in subsequently smaller remnant strains S_r with increasing load. In addition to strain originating from ferroelasticity, there is also an elastic response, S_{elastic}, that has to be considered as well. For an elastic material, the mechanical constitutive equation in tensorial notation is given as [39]

$$S_{ij} = s_{ijkl}\sigma_{kl} \tag{2}$$

where S_{ij} and σ_{kl} are the strain and stress tensors, respectively, and s_{ijkl} are the elastic compliances. In this study, only the deformation along the uniaxial load is considered, allowing the relationship to be simplified to

$$S_{33} = s_{3333}\sigma_{33} = (1/E)\sigma_{33} \tag{3}$$

where E is the Young's modulus parallel to the load. This analysis relies on the assumption that the Young's modulus is not a function of stress and thus ferroelastic domain texture. However, it has been previously shown for PZT using partial unloading experiments that the macroscopic Young's modulus of the ceramic evolves during mechanical loading due to the anisotropy of the single crystal elastic properties [29,40,41]. Here, since high-quality elastic data for BCTZ is not available and all investigated compositions appear to be ultrasoft compared to soft PZT (Fig. 5), the Young's modulus E is determined by a linear regression of the strain data under high stress. It is understood that this assumption will lead to error, as the Young's modulus changes with stress; however, due to the low coercive stress of the current compositions (10–25 MPa) compared to the maximum applied stress (250 MPa), the error should be minimal and will not affect the conclusions. Deviations are only expected at small stresses, below 10–25 MPa, for which an inflection point in the strain–stress data is observed. Previous experimental measurements of soft PZT showed an increase in Young's modulus by a factor of 3 [29], which would lead to an error of $\Delta S_{\mathrm{elastic}} < 0.05\%$ in the current study, where the Young's modulus increases linearly from 40 to 120 GPa for stresses up to 100 MPa.

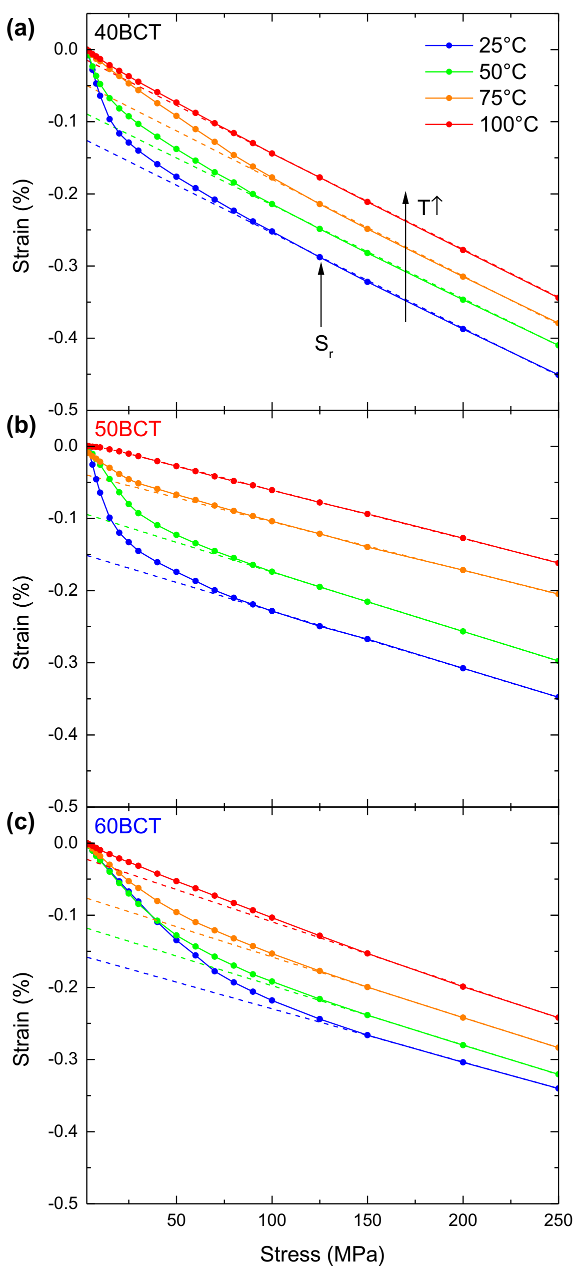

Fig. 5. The values for the remnant strain, S_r, at 25, 50, 75 and 100 °C for (a) 40BCT, (b) 50BCT and (c) 60BCT (top to bottom). The linear fits at high compressive stresses allow quantification of the elastic component of the strain.

With this assumption, the total strain under the compressive load can then be written as

$$S_r = S_{\mathrm{elastic}} + S_{\mathrm{ferroelastic}} = (1/E)\sigma + S_{\mathrm{ferroelastic}} \tag{4}$$

where the stress-dependent Young's modulus can be determined from the evolution of the remnant strain with stress. This allows for the stress-induced ferroelastic strain $S_{\mathrm{ferroelastic}}$ contribution to be directly determined and compared to the electric field-induced strain.

The remnant strains S_r for (a) 40BCT, (b) 50BCT and (c) 60BCT are provided in Fig. 5 as a function of the stress σ at 25, 50, 75 and 100 °C. The non-linear strain at low σ represents the stress-induced ferroelastic strain $S_{\mathrm{ferroelastic}}$, which is most prominent at 25 °C and decreases at higher temperatures as the structural distortions become smaller when approaching T_c. The slope at higher σ is composed exclusively of the elastic component, as it is expected that most non-180° domains will have already switched. By fitting the curves between 100 and 250 MPa in 40BCT and 50BCT, and between 150 and 250 MPa in 60BCT, the elastic moduli can be extracted from the slope and the maximum ferroelastic strain from the intercept. All fits have an adjusted $R^2 > 0.999$, which translates to a fit with $\Delta E < 0.01$ and $\Delta S_{\mathrm{ferroelastic}} < 0.004\%$. The range of the determined moduli originates from the measurements at the different temperatures, for which the materials soften elastically near the phase transition temperatures [19]. Table 1 lists the relevant fitting parameters $S_{\mathrm{ferroelastic}}$ and E for all compositions and temperatures. At 25 °C, the E values were found to be 76, 126 and 135 GPa for 40BCT, 50BCT and 60BCT, respectively. The achievable ferroelastic strains $S_{\mathrm{ferroelastic}}$ are −0.12%, −0.15% and −0.16%, respectively.

In order to determine what volume fraction of non-180° domains switch under the compressive stress, the ferroelastic domain texture f_{002}, expressed in multiples of random distribution, is calculated for the tetragonal 60BCT material. In tetragonal materials f_{002} varies between 0 and 3, where 0 means that none of the domains are aligned in the direction of interest, 1 corresponds to a random orientation and 3 signifies that all of the domains are aligned in that direction [42]. The f_{002} is calculated from $S_{\mathrm{ferroelastic}}$ using the relationship [43]

$$S_{\mathrm{ferroelastic}} = \int_0^{\pi/2} (c/a - 1)(f_{002}(\alpha) - 1)\cos^2\alpha \sin\alpha d\alpha \tag{5}$$

Table 1
Elastic moduli E and maximum ferroelastic strains $S_{\text{ferroelastic}}$ parallel to the load as determined from linear regression in Fig. 5.

	40BCT		50BCT		60BCT	
	E (GPa)	$S_{\text{ferroelastic}}$ (%)	E (GPa)	$S_{\text{ferroelastic}}$ (%)	E (GPa)	$S_{\text{ferroelastic}}$ (%)
25 °C	76	−0.12	126	−0.15	135	−0.16
50 °C	77	−0.09	122	−0.09	122	−0.12
75 °C	75	−0.05	149	−0.04	119	−0.07
100 °C	75	−0.01	149	0.01	112	−0.02

where σ is the orientation angle and the c/a ratio describes the lattice distortion of the tetragonal unit cell, reported to be 1.006 at room temperature for 60BCT [44]. The $S_{\text{ferroelastic}}$ under the mechanical stress is −0.16%. The ferroelastic domain texture f_{002} is a function of the orientation σ to the applied stimulus and can be described by the March–Dollase orientation probability distribution function [45],

$$P(r,\alpha) = \left(r^2\cos^2\alpha + \frac{1}{r}\sin^2\alpha\right)^{-3/2} \tag{6}$$

The parameter r for a material with a fibrous texture is given by $r = f_{002}^{-1/3}$ [46]. Here, f_{002} is the ferroelastic domain texture parallel to the stimulus, i.e. the applied mechanical stress. Solving the integral numerically, with the parameters $S_{\text{ferroelastic}} = -0.16\%$ and $c/a = 1.006$ and the March–Dollase function, yields $f_{002} < 0.1$ parallel to the applied stress. This means that less than 3% of the non-180° domains are aligned with their c-axis in the direction of the mechanical load at the maximum applied stress. Note that, for this approximate calculation, it was assumed that the March–Dollase function accurately describes the orientation distribution of the non-180° domains and that the lattice distortion c/a is independent of the orientation σ and applied mechanical stresses and electric fields. Variations in c/a have been found to depend on the orientation as well as the applied electric field [44,47,48] and stress [49]. The current results, however, indicate that nearly all of the domains have been switched into a direction perpendicular to the stress axis at stresses $\sigma > 150$ MPa. This is supported by the observed linear strain response at stresses larger than 150 MPa, which suggests a saturated ferroelastic contribution. This agrees well with results from in situ XRD data showing the strong susceptibility of non-180° domain wall motion under an applied electric field [44]. A similar sensitivity is expected under stress. Because the tetragonal 60BCT has the largest coercive stress of the investigated compositions, it can be assumed that the nearly complete alignment of non-180° domains perpendicular to the stress and electric field directions also occurs for 40BCT and 50BCT.

3.4. Mechanism

In order to illustrate the competition between stress-induced ferroelastic switching and the field-induced domain alignment, the elastic component determined above is subtracted from the remnant strain S_r and the maximum strain $S_{\max}$. The absolute stress-induced ferroelastic strain is then given by

$$S^{\sigma}_{\text{ferroelastic}}(\sigma) = S_r(\sigma) - (1/E)\sigma \tag{7}$$

The $S^{\sigma}_{\text{ferroelastic}}$ represents the cumulative strain at stress σ and zero field without the elastic contribution. $S^{\sigma}_{\text{ferroelastic}}$ approximately corresponds to the purely stress-induced non-180° domain switching strain. In the limit of large stresses, it is equal to the intercept of the linear regression of the elastic strain (Fig. 5) and is expected to saturate once all the non-180° domains have switched perpendicular to the stress direction. The absolute field-induced strain is given by

$$S^{E}(\sigma) = S_{\max}(\sigma) - (1/E)\sigma \tag{8}$$

Note that S^E consists of intrinsic piezoelectric, extrinsic domain switching and electrostrictive components. Similarly to $S^{\sigma}_{\text{ferroelastic}}$, S^E represents the cumulative strain at stress σ and under a maximum field without including the elastic contribution. Eqs. (7) and (8) can now be combined to compute S_u, where $S_u = S_{\max} - S_r$. The two curves, $S^{\sigma}_{\text{ferroelastic}}$ and S^E, are shown in Fig. 6 for (a) 40BCT, (b) 50BCT and (c) 60BCT at 25, 50, 75 and 100 °C for the field amplitude of 2 MV m^{-1}. The full symbols represent $S^{\sigma}_{\text{ferroelastic}}$ and the open symbols represent S^E. $S^{\sigma}_{\text{ferroelastic}}$ represents the absolute strain due to stress-induced non-180° domain switching, while S^E represents the absolute strain under 2 MV m^{-1}. The difference between the curves then corresponds to the achievable unipolar strain S_u that is maximized for optimum performance, as $S^E - S^{\sigma}_{\text{ferroelastic}} = S_{\max} - S_r = S_u$.

Large values of $S_u/E_{\max}$ with pronounced maxima at stresses between 8 and 30 MPa (Fig. 4) are observed in 40BCT at 25 and 50 °C and in 50BCT between 25 and 75 °C. This implies that the stress-induced domain switching is reflected more strongly in $S^{\sigma}_{\text{ferroelastic}}$ compared to S^E, which is indicated by steeper $S^{\sigma}_{\text{ferroelastic}}$ curves compared to S^E, i.e. $\left|dS^{\sigma}_{\text{ferroelastic}}/d\sigma\right| > \left|dS^E/d\sigma\right|$ in Fig. 6. As a result, the distance between both curves increases and thus also S_u. This occurs under small compressive stresses. In that region the strain response is field controlled, because the electric field dominates the electromechanical performance of the material. The limit of this regime is indicated by a change in slope of $S^{\sigma}_{\text{ferroelastic}}$ occurring at the maximum of $S_u/E_{\max}$ and is highlighted here with arrows. At stresses above this limit and higher temperatures, the $S^{\sigma}_{\text{ferroelastic}}$ is not steeper than S^E and the two curves approach each other

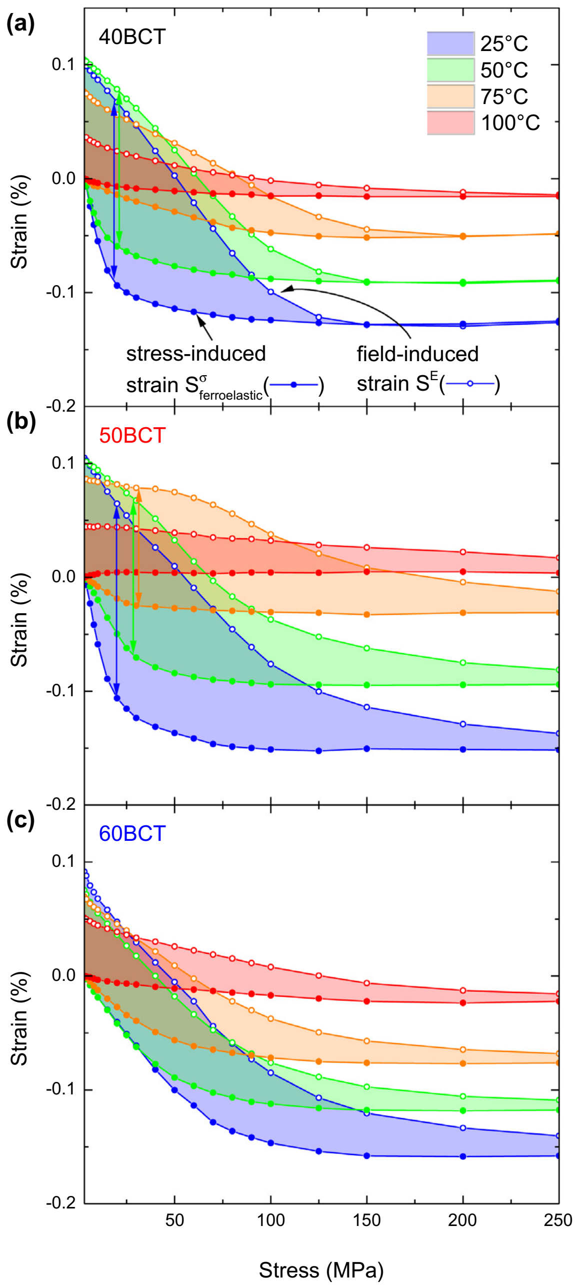

Fig. 6. The competition between the stress-induced ferroelastic strain (full symbols) and field-induced strain (open symbols) at 2 MV m^{-1} are shown at 25, 50, 75 and 100 °C for (a) 40BCT, (b) 50BCT and (c) 60BCT (top to bottom). The elastic components have been subtracted. The maximum electromechanical properties are observed when the slope of the stress-induced strain component is steeper than the slope of the field-induced strain component.

with increasing stress. This means that the electromechanical response is stress-controlled, because the electric-field-induced domain alignment is significantly suppressed due to stress induced domain clamping.

The field-controlled regime occurs in 40BCT at 25 and 50 °C and in 50BCT between 25 and 75 °C. In 60BCT, a similar field-controlled regime does not exist and hence the electromechanical performance is not as large. The difference between the different compositions could arise from possible field-induced symmetry changes in the vicinity of the MPB that are not available in the tetragonal material.

The stress-controlled regime is pronounced in 40BCT, where the unipolar strain is clamped at zero at larger stresses. In 50BCT and 60BCT, on the other hand, a finite strain remains even at 250 MPa. This is likely due to the piezoelectric and electrostrictive components that are active even when all non-180° domains have already switched. The strain that is still observed at 100 °C is mainly due to electrostriction as the materials are in their paraelectric state.

4. Conclusions

Extraordinarily large field-induced strains with large signal piezoelectric coefficients of up 1540 pm V^{-1} are measured for BCTZ compositions across the MPB. The largest piezoelectric coefficients, expressed in terms of the unipolar strain divided by the field amplitude, S_u/E_{max}, are found for 40BCT and 50BCT, while the tetragonal 60BCT shows smaller values at all temperatures. Increased uniaxial compressive stresses lead to an initial increase in the piezoelectric coefficient displaying a maximum for stresses between 8 and 30 MPa, depending on composition, temperature and field amplitude. A further increase in the stress gradually suppresses the field-induced strain response. Moreover, in 40BCT an electric threshold field is required to overcome the stress-induced domain clamping and obtain a measurable strain response. The threshold field increases almost linearly with increasing stress and exceeds 2 MV m^{-1} at 150 MPa. At elevated temperatures, the threshold field becomes smaller as the structural distortions are reduced. By adjusting the composition, stress and electric field amplitude a region is identified in which piezoelectric coefficients between 740 and 1540 pm V^{-1} can be achieved for temperatures between at least 25 and 75 °C. By subtracting the elastic contribution from the total strain, the pure stress-induced and field-induced domain switching strains are quantified. The maximum strain response is found in the field-controlled regime, in which stress-induced domain alignment in the direction perpendicular to the stress occurs, but at the same time the electric field still can overcome the stress-induced domain clamping. Hence, in the field-controlled regime there are more domains available that can be realigned back into the electric field direction, resulting in the extraordinary large strains.

Acknowledgements

This work was supported by the United States National Science Foundation under Award No. DMR 0805022 and the Deutsche Forschungsgemeinschaft DFG under WE 4972/1-1.

References

[1] Uchino K. Ferroelectric devices. New York: Marcel Dekker; 2000.
[2] Moulson AJ, Herbert JM. Electroceramics: materials, properties, applications. Chichester: Wiley; 2003.
[3] Jaffe B, Cook WR, Jaffe H. Piezoelectric ceramics. London: Academic Press; 1971.
[4] Jo W, Dittmer R, Acosta M, Zang J, Groh C, Sapper E, et al. J Electroceram 2012;29:71.
[5] Directive 2011/65/EU: the restriction of the use of certain hazardous substances in electrical and electronic equipment (RoHS), 2011, OJ L174/88.
[6] Directive 2012/19/EU: waste electrical and electronic equipment (WEEE), 2012, OJ L197/38.
[7] Ministry of Economy, Trade and Industry, Japan: 2001.
[8] Ministry of Information Industry, China: 2007.
[9] Environment and Labor Committee of the National Assembly of Korea: 2007.
[10] Department of Toxic Substances Control, California, USA: 2003.
[11] Saito Y, Takao H, Tani T, Nonoyama T, Takatori K, Homma T, et al. Nature 2004;432:84.
[12] Damjanovic D, Klein N, Li J, Porokhonskyy V. Funct Mater Lett 2010;3:5.
[13] Rödel J, Jo W, Seifert KTP, Anton E-M, Granzow T, Damjanovic D. J Am Ceram Soc 2009;92:1153.
[14] Panda P. J Mater Sci 2009;44:5049.
[15] Liu W, Ren X. Phys Rev Lett 2009;103:257602.
[16] Ehmke MC, Ehrlich SN, Blendell JE, Bowman KJ. J Appl Phys 2012;111:124110.
[17] Haugen AB, Forrester JS, Damjanovic D, Li B, Bowman KJ, Jones JL. J Appl Phys 2013;113:014103.
[18] Keeble DS, Benabdallah F, Thomas PA, Maglione M, Kreisel J. Appl Phys Lett 2013;102:092903.
[19] Damjanovic D, Biancoli A, Batooli L, Vahabzadeh A, Trodahl J. Appl Phys Lett 2012;100:192907.
[20] Damjanovic D. Appl Phys Lett 2010;97:062906.
[21] Randall CA, Kelnberger A, Yang GY, Eitel RE, Shrout TR. J Electroceram 2005;14:177.
[22] Uchino K, Takahashi S. Curr Opin Solid State Mater Sci 1996;1:698.
[23] Janocha H. Adaptronics and smart structures: basics, materials, design and applications. Berlin: Springer; 2007.
[24] Dittmer R, Aulbach E, Jo W, Webber KG, Rödel J. Scr Mater 2012;67:100.
[25] Webber KG, Aulbach E, Rödel J. J Phys D Appl Phys 2010;43:365401.
[26] Dittmer R, Webber KG, Aulbach E, Jo W, Tan X, Rödel J. Sens Actuators A 2013;189:187.
[27] Dittmer R, Webber KG, Aulbach E, Jo W, Tan X, Rödel J. Acta Mater 2013;61:1350.
[28] Ehmke MC, Daniels J, Glaum J, Hoffman M, Blendell JE, Bowman KJ. J Appl Phys 2012;112:114108.
[29] Webber KG, Aulbach E, Key T, Marsilius M, Granzow T, Rödel J. Acta Mater 2009;57:4614.
[30] Schäufele AB, Härdtl KH. J Am Ceram Soc 1996;79:2637.
[31] Cao H, Evans AG. J Am Ceram Soc 1993;76:890.
[32] Lynch CS. Acta Mater 1996;44:4137.
[33] Zhou D, Kamlah M, Munz D. J Mater Res 2004;19:834.
[34] Chaplya PM, Carman GP. J Appl Phys 2002;92:1504.
[35] Li YW, Zhou XL, Li FX. J Phys D Appl Phys 2010;43:175501.
[36] Zhou D, Kamlah M, Munz D. J Eur Ceram Soc 2005;25:425.
[37] Mitrovic M, Carman GP, Straub FK. Int J Solids Struct 2001;38:4357.
[38] Kerkamm I, Hiller P, Granzow T, Rödel J. Acta Mater 2009;57:77.
[39] Nye JF. Physical properties of crystals: their representation by tensors and matrices. New York: Oxford University Press; 1985.
[40] Fett T, Munz D, Thun G. Ferroelectrics 2002;274:67.
[41] Zhou D, Wang R, Kamlah M. J Eur Ceram Soc 2010;30:2603.
[42] Jones JL, Iverson BJ, Bowman KJ. J Am Ceram Soc 2007;90:2297.
[43] Jones JL, Hoffman M, Bowman KJ. J Appl Phys 2005;98:024115.
[44] Ehmke MC, Khansur N, Daniels J, Blendell JE, Bowman KJ. Acta Mater 2014;66:340.
[45] Dollase WA. J Appl Crystallogr 1986;19:267.
[46] Lee SB, Key TS, Liang Z, García RE, Wang S, Tricoche X, et al. J Eur Ceram Soc 2013;33:313.
[47] Hinterstein M, Rouquette J, Haines J, Papet P, Knapp M, Glaum J, et al. Phys Rev Lett 2011;107:077602.
[48] Daniels JE, Jo W, Rödel J, Honkimäki V, Jones JL. Acta Mater 2010;58:2103.
[49] Jones JL, Hoffman M, Vogel SC. Mech Mater 2007;39:283.